Low temperature oxidation of amorphous silicon nanoparticles

Feiyu Xu, Brandon Wagner ⬡, Pankaj Ghildiyal, Lorenzo Mangolini ⬡, and Michael R. Zachariah[*]
University of California, Riverside, California 92551, USA

The oxide layer is important for the processing and applications of silicon nanoparticles as it provides chemical stability to the material. Herein, the thermal oxidation of sub-10-nm crystalline and amorphous silicon particles in dry air is investigated with nonisothermal kinetic analysis including Kissinger and Flynn-Wall-Ozawa methods at various heating rates. The results indicate that amorphous silicon nanoparticles have a considerably lower activation energy for oxidation (98 kJ/mol) compared to their crystalline counterparts (182 kJ/mol). *In situ* heating diffuse reflectance infrared Fourier transform spectroscopy was employed to monitor the evolution of surface species of Si nanoparticles during oxidation. The results suggest that backbond oxidation of higher hydrides contribute to the low onset temperature for oxidation of amorphous silicon nanoparticles. Besides, surface O_3Si-H and Si-OH species likely prevent the formation of a dense silicon oxide layer, resulting in the low temperature oxidation behavior of amorphous silicon nanoparticles. These results provide insight into kinetics and chemistry of amorphous silicon oxidation in the thin film regime.

I. INTRODUCTION

Silicon nanostructures have found applications in transistors, photovoltaics, lithium-ion batteries, bioimaging, energetic materials, and many other areas, due to their unique properties [1–7]. The Si/SiO_2 interface is also a subject of interest as SiO_2 can act as a passivation layer for silicon, and it alters the electronic and optical properties of silicon nanocrystals [8]. In addition, with increasing demand for high performance processors and miniaturization of electronics, the ability to grow an ultrathin SiO_2 layer with precise control has become increasingly critical in semiconductor industry [9]. The SiO_2 shell affects the energy release rate of silicon nanoparticles in nanoenergetic materials as well [10]. Therefore, a better understanding of the oxidation of silicon nanostructures would benefit a variety of applications.

Oxidation of silicon has a long history of study [11–20]. Deal and Grove developed the classic linear-parabolic model for the oxidation of silicon films [21]. It states that oxygen dissolves and migrates through a silicon oxide layer to react with silicon at the silicon/silicon oxide interface. This model describes the oxidation of thick silicon films accurately, but for thin oxides (less than a few hundred angstroms), the experimentally obtained oxidation rate is higher than that predicted by the Deal-Grove model [22]. The Deal-Grove model also fails to accurately predict oxidation rate in nanoparticles or nanowires. For Si nanoparticle oxidation, Liao *et al.* [23] considered two regimes of thermal oxidation of crystalline Si nanoparticles. The first regime is the fast surface oxidation through direct contact with oxygen. After surface oxidation, an oxide layer of a critical thickness which inhibits oxygen diffusion will form, and oxidation becomes diffusion limited. The second regime is the diffusion-controlled growth of the oxide layer at high temperature. As differences in dimensions of silicon structures often lead to discrepancies in oxidation behavior, it is necessary to investigate oxidation of silicon at various length scales.

The oxidation kinetics of silicon particles of a few nanometers in size has not been studied extensively, in part due to the difficulty in measuring the oxide thickness in an accurate way [24]. However, the results would provide useful information for examining silicon oxide growth in the thin film regime as well as surface reactivity of silicon nanocrystals. In this work, thermogravimetric analysis was used to investigate the oxidation of nonthermal plasma-synthesized sub-10-nm Si (nSi) particles in dry air. In particular, we focus on amorphous nSi (*a*-nSi) because its oxidation is even less characterized than that of crystalline nSi (*c*-nSi). We have found that *a*-nSi particles show unique low temperature oxidation behavior compared to their crystalline counterparts. Activation energy for oxidation of nSi particles were estimated from nonisothermal measurements at various heating rates using Kissinger and Flynn-Wall-Ozawa methods [25–27]. Both methods show a consistent result that *a*-nSi particles have a much lower energy barrier for oxidation compared to crystalline particles. *In situ* heating diffuse reflectance infrared Fourier transform spectroscopy (DRIFTS) was utilized to elucidate the underlying chemistry for this behavior. The results indicate that backbond oxidation of surface hydrides is responsible for the initial rapid oxidation of *a*-nSi particles. Besides, the presence of O_3Si-H and Si-OH groups likely prevents the growth and formation of a dense SiO_2 layer as oxygen barrier, as evidenced by the unique behavior and low completion temperature for oxidation of *a*-nSi particles.

II. EXPERIMENT

A. Materials

Silicon nanoparticles were synthesized with a nonthermal plasma reactor (see Fig. S1 of the Supplemental Material

---

*mrz@engr.ucr.edu

for detailed reactor setup [28]) [29]. Inherent to nonthermal plasma synthesis, gas molecules are ionized and reactions between neutral species and ions occur to produce particles. For the case of silane plasmas, silane is ionized through electron collisions with the gas molecules, creating silyl and silylene radicals that react with neutral silane to produce Si clusters. These clusters proceed to grow through chemical reactions with neutral silicon hydrides [30]. Subsequently, surface growth of the Si NPs occurs via chemical vapor deposition where the larger, negatively charged Si NPs react with neutral or positively charged silicon hydrides [31]. Surface heating of the particles happens via electron-ion recombination and surface hydrogen reactions, which promote crystallization of the Si NPs [29]. Quartz tube (8×1 in.) was used for the plasma reactor. Two copper ring electrodes were separated by 1 in. and placed 1 in. from the upstream stainless-steel flange. The rings were connected to an rf power supply (RFPP RF5S) and matching network (MFJ Versa Tuner V). A butterfly valve was utilized to maintain a constant pressure of 3.5 Torr, and a 100-Torr baratron (MKS Baratron Capacitance Manometer) was used to monitor the pressure within the reactor. Silane (1.36% SiH_4 in Ar) was flown as the precursor gas (200 sccm) while the rf input power was varied from 10 to 50 W at 13.56 MHz to produce *a*-Si and *c*-Si NPs, respectively. The estimated residence time within the plasma reactor, based on flow velocity, was ~ 97 ms. The particles were collected downstream of the plasma volume by filtering.

B. Characterizations

TEM (120-kV accelerating voltage; Thermo Fisher Scientific Talos L120C) was used to analyze the size of the particles. The instrument is equipped with a thermionic electron gun (LaB_6 cathode), TWIN objective lens (0.20-nm line resolution), and a CETA 16 (4 K$\times$4 K complementary metal-oxide semiconductor) camera for digital imaging. Images from TEM were used in ImageJ (v1.53e) to measure particle diameters for size analysis. The scale bar from the TEM image was used to set the scale according to the pixel to distance ratio. TEM grids were coated directly from the flow-through plasma reactor by exposing the grids for particle collection for ~ 1 s. High-resolution TEM (HRTEM) (Thermo Fisher Scientific Titan Themis 300) was performed to obtain high-resolution images of the Si NPs with apparent lattice planes. This instrument is equipped with a X-FEG electron gun, STWIN objective lens (0.2-nm TEM point resolution), and a FEI CETA II (4 K $\times$ 4 K charge coupled device) camera for digital imaging. x-ray diffraction (XRD) [Empyrean PANalytical Series 2; Cu-$K\alpha$ source ($\lambda = 1.541$ Å)] was used for determining the crystallinity of the particles. The divergence slit was 0.76 mm and a Si substrate background was used for the measurements. Thermogravimetric analysis (TGA) was performed using a Netzsch Jupiter STA F3 thermal analyzer. An environmental chamber was used to perform Fourier transform infraredmeasurement in diffuse reflectance as a function of temperature (Harrick Scientific Products: Praying Mantis Diffuse Reflection Accessory and Praying Mantis High Temperature Reaction Chamber HVC-DRM-5; temperature range: $100-600\,^{\circ}C$).

III. RESULTS AND DISCUSSION

High-resolution transmission electron microscopy (HRTEM) image of *a*-nSi particles and the corresponding FFT pattern [Fig. 1(a)] show that there is no sign of crystal ordering, confirming the amorphous nature of the particles. For comparison, *c*-nSi particles were also prepared using the same method but at a higher plasma power (see Fig. S2 of the Supplemental Material for TEM analysis [28]). The particles have apparent lattice planes according to the Si (111) plane. Crystallization is induced by higher particle temperature associated with the higher plasma power [32]. The average size of the particles is 5.6 ± 1.2 and 6.0 ± 1.5 nm for *a*-nSi and *c*-nSi particles, respectively, as determined from TEM images [Figs. 1(c) and 1(d)]. XRD patterns of *a*-nSi and *c*-nSi particles are shown in Fig. 1(b). *a*-nSi particles show a broadening of peaks due to lack of long-range order of Si atoms. According to Scherrer's analysis of the XRD pattern from the *c*-nSi particles, the calculated size is 4.84 nm. This lies within the particle size distribution for the *c*-nSi sample according to TEM. To better understand the crystalline degree of the prepared *c*-nSi particles, the fraction of crystalline material in *c*-nSi particles was estimated by a method proposed by Lopez *et al.* [33], where peak position and width of amorphous Si peaks are held constant while fitting their amplitude together with three crystalline Si peaks. The crystalline fraction is calculated as the peak area under three crystalline peaks over the total area. Result shows 62% crystalline of the prepared *c*-nSi particles.

Thermal oxidation of nSi particles was studied using thermogravimetric analysis. To avoid contact with air, prepared nSi particles were transferred directly to a glove box after synthesis, where they were sealed in glass vials in nitrogen. However, the samples were briefly exposed to air due to sample loading and weighing before TGA measurements start. The oxidation experiments were carried out in synthetic air (21% O_2; 79% N_2) from 25 to $1200\,^{\circ}C$ under various heating rates ($2.5/5/10/20\,^{\circ}C/$ min). The mass change profiles, along with their first derivatives (DTG), are shown in Fig. 2.

By comparing Figs. 2(a) and 2(b), it is apparent that the temperature range during which oxidation occurs is different for amorphous and crystalline nSi particles. For *a*-nSi, the oxidation initiates at $\sim 100\,^{\circ}C$ and completes at $\sim 600\,^{\circ}C$, while for *c*-nSi, the temperature range for oxidation is approximately $200-1000\,^{\circ}C$. These temperature values vary slightly with heating rates. Assuming that Si is converted to SiO_2 after complete oxidation, the Si content in nSi particles prior to TGA measurements can be calculated from the final mass of the samples:

$$\omega_{Si} = \frac{(m' - m_0)/m_0}{(M_{SiO_2} - M_{Si})/M_{Si}}, \qquad (3.1)$$

where ω_{Si} is the initial mass fraction of Si in the nSi particles, m' is the final mass of the samples, m_0 is the initial mass of the samples, and M_{SiO_2} and M_{Si} are the molar mass of SiO_2 and Si, respectively. The results show that the Si content is about 69–75% for *a*-nSi particles, and 86–92% for *c*-nSi particles. This suggests that despite the precautions taken, oxide has formed before measurements, especially for *a*-nSi particles. This is likely due to the unpassivated silicon dangling bonds
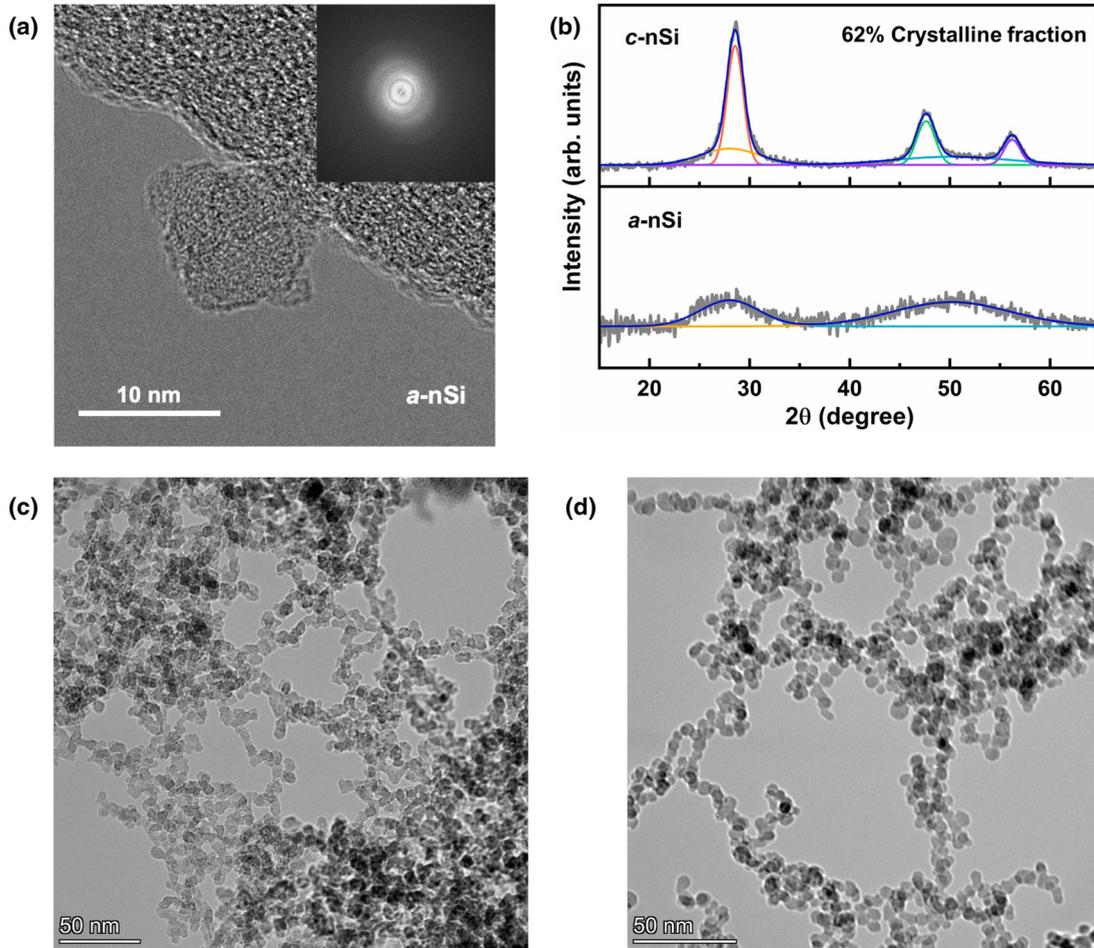
FIG. 1. (a) HRTEM of a-nSi particles. (b) XRD of a-nSi and c-nSi particles. TEM images of (c) a-nSi and (d) c-nSi particles.

formed in the plasma, which are highly reactive and will oxidize rapidly in the presence of oxygen or water.

The first derivatives of the TG curves are plotted in Figs. 2(c) and 2(d), in which $d\alpha/dt$ represents the oxidation rate. The temperature dependence of the oxidation rate clearly indicates that several thermally activated processes are involved in the oxidation reaction. Furthermore, the oxidation patterns are distinctly different for a-nSi and c-nSi, as demonstrated by the shape of the DTG curves. The DTG results suggest that the oxidation of a-nSi particles proceeds initially through a very rapid reaction that reaches maximum rate at $\sim 220\,^\circ$C, followed by two subsequent steps at around 380 and 480 $^\circ$C, respectively. These steps are in a large part overlapped. By contrast, c-nSi shows three distinct oxidation steps at low, intermediate, and high temperature ranges, evidenced by the peaks at around 280, 650, and 880 $^\circ$C, respectively. The differences reflect different underlying oxidation mechanisms and will be discussed further.

Many previous studies of silicon oxidation use isothermal methods to obtain kinetic parameters, as the oxidation of bulk phase silicon typically occurs at high temperature [13,21,34]. However, due to the large surface area and unique surface chemistry leading to low onset temperature and wide temperature range within which oxidation occurs, isothermal measurements cannot capture the broad range of oxidation regimes observed in as-prepared nSi particles. Therefore, in

the present study we will utilize nonisothermal kinetic analysis to investigate the oxidation of nSi particles.

In thermal analysis of solids, the reaction rate is considered as a function of temperature (T) and extent of the reaction (α) [35]. For thermally stimulated processes, the reaction rate also follows an Arrhenius relationship. With a linear temperature ramp, the temperature dependence of process rate can be expressed as

$$\beta \frac{d\alpha}{dT} = A\exp\left(\frac{-E_a}{RT}\right)f(\alpha), \qquad (3.2)$$

where β is the heating rate, A is the pre-exponential constant, E_a is the activation energy, R is the universal gas constant, and $f(\alpha)$ is the reaction model.

A simple and widely applied method for estimating activation energy in thermal analysis is the Kissinger method [25]. The Kissinger method is derived under the condition that at maximum reaction rate,

$$\frac{d^2\alpha}{dt^2} = 0. \qquad (3.3)$$

After rearrangement, the Kissinger equation is obtained:

$$\ln\left(\frac{\beta}{T_m^2}\right) = \ln\left(\frac{-AR}{E_a}f'(\alpha_m)\right) - \frac{E_a}{RT_m}. \qquad (3.4)$$
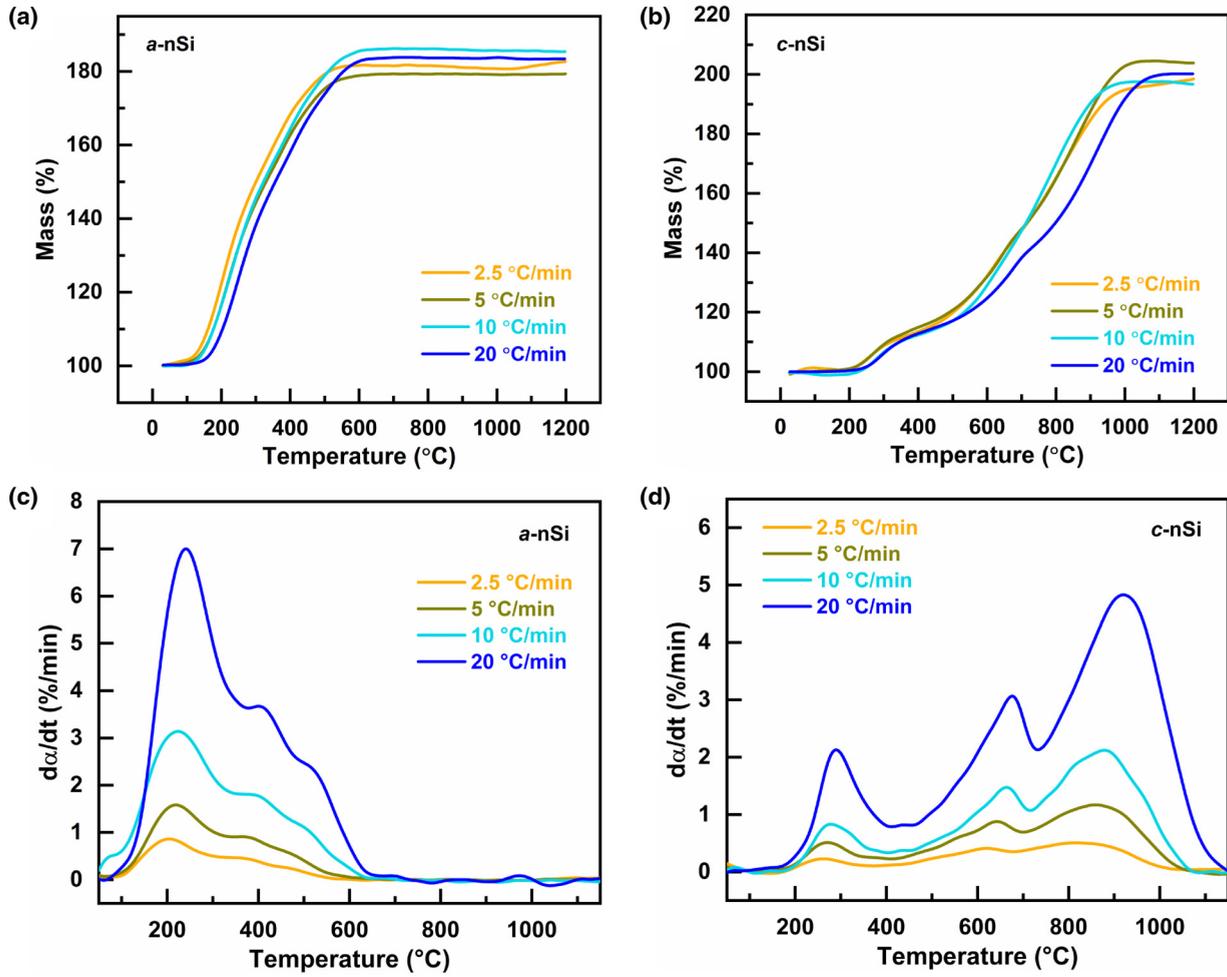
FIG. 2. TG curves of (a) *a*-nSi and (b) *c*-nSi, and DTG curves of (c) *a*-nSi and (d) *c*-nSi particles.

Here, T_m refers to the temperature at which oxidation rate reaches maximum for the initial oxidation. The Kissinger method was applied using data at various heating rates, by plotting the left side of Kissinger equation $\ln(\frac{\beta}{T_m^2})$ against $1000/T_m$. The results are shown in Fig. 3. From the slope of the Kissinger plot, the activation energy can be estimated.
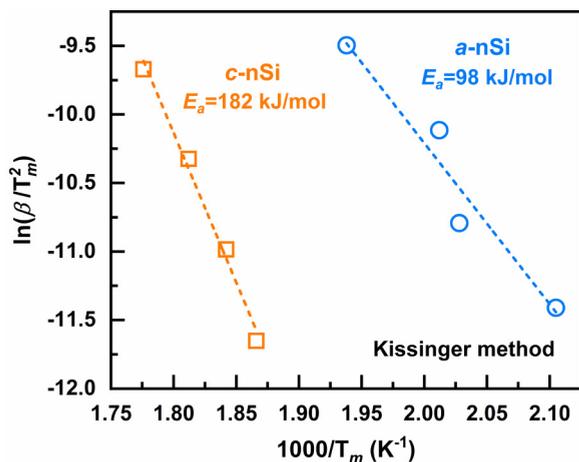
FIG. 3. Kissinger plot for oxidation of *a*-nSi and *c*-nSi particles.

The E_a for oxidation onset is calculated to be 98 and 182 kJ/mol for *a*-nSi and *c*-nSi, respectively. This indicates that at the initial stage of oxidation, *a*-nSi has a significantly lower energy barrier, consistent with its lower onset temperature and higher reaction rate.

The simplicity of the Kissinger method comes with certain limitations, the most prominent one being that it yields a single value for activation energy regardless of the complexity of the reaction. Moreover, for most reaction models (that are not first order), the intercept of the Kissinger plot is not a constant, because $f'(\alpha_m)$ is dependent on α_m, and thus β. But the error caused by this is usually negligible [35,36].

Since the oxidation process of nSi particles involves multiple thermally activated processes, the Flynn-Wall-Ozawa (FWO) isoconversional method was also applied to study the conversion dependence of activation energy [26,27]. This relationship often provides insights into the reaction mechanism and a cross check of the Kissinger results. Isoconversional methods are based on the principle that the reaction rate at constant extent of conversion α is only a function of temperature. Applying this principle to the integral form of Eq. (3.2) leads to the equation

$$g(\alpha) = \frac{A}{\beta} \int_0^T \exp\left(\frac{-E_\alpha}{RT}\right) dT. \tag{3.5}$$
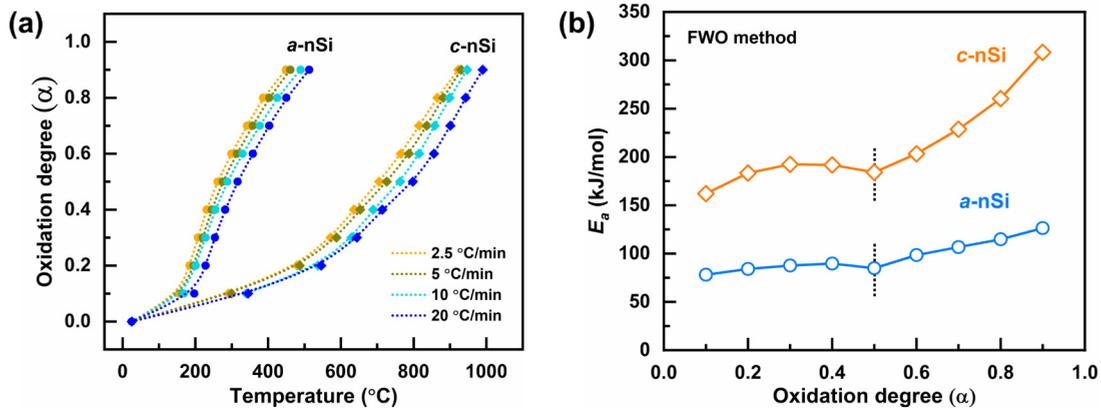
FIG. 4. (a) Temperature dependence of oxidation degree. (b) Relationship between E_a and α.

Equation (3.5) does not have an analytical solution, which results in various integral isoconversional methods that differ in the approximation of the temperature integral. The FWO method adopts the approximation by Doyle [37] and gives the following equation:

$$\ln(\beta_i) = \text{Const} - 1.052\left(\frac{E_\alpha}{RT_\alpha}\right). \quad (3.6)$$

The subscript α denotes that the value corresponds to a specific conversion degree. To apply the FWO method, the TG data are first converted to an oxidation degree [Fig. 4(a)] that represents the extent of the conversion of the oxidation reaction. By using the data from Fig. 4(a) and plotting $\ln(\beta_i)$ vs $1/T_\alpha$, the slope of the linear fitting can be used to evaluate E_a. The dependence of E_a on oxidation degrees are illustrated in Fig. 4(b). The results show that for a-nSi, the initial activation energy is 78 kJ/mol, which slightly increases to 90 kJ/mol for $\alpha = 0.4$. After a dip to 85 kJ/mol for $\alpha = 0.5$, E_a increases monotonically to 126 kJ/mol at $\alpha = 0.9$. For c-nSi, E_a starts at a much higher value of 162 kJ/mol. Then it follows a similar trend where it increases to 192 kJ/mol ($\alpha = 0.4$), dips to 184 kJ/mol ($\alpha = 0.5$), and increases again to 308 kJ/mol ($\alpha = 0.9$). Overall, the activation energy for oxidation is significantly higher for c-nSi. The activation energies of both samples share a trend where E_a remains relatively constant before $\alpha = 0.5$; after that, E_a starts to increase significantly. The corresponding E_a values obtained from the FWO method (90 and 162 kJ/mol) are similar to those estimated using the Kissinger method (98 and 182 kJ/mol), confirming the validity of the results.

$\alpha = 0.5$ seems to be a transition point for oxidation regimes and requires further analysis. It has been proposed that there are two regimes for thermal oxidation of crystalline Si nanoparticles prepared by plasma [23]. First is the fast surface oxidation of silicon via direct contact with oxygen, after which an oxide layer of a critical thickness will form and act as an oxygen barrier. The oxidation is then transformed to an oxygen diffusion-controlled process. Assuming particles are spherical, the total oxide layer (native oxide + oxide growth) thickness corresponding to $\alpha = 0.5$ can be estimated to be about 0.8 and 0.7 nm for a-nSi and c-nSi particles, respectively. This is close to the typical thickness (1 nm) of the native oxide shell of Si particles after long-term exposure to air [38].

Based on the above discussion, we hypothesize that before α reaches 0.5, i.e., the formation of an oxide layer with critical thickness, the oxidation is dominated by surface reactions. After the formation of the critical oxide layer, the increasing E_a of c-nSi indicates diffusion controlled self-limiting oxide growth, whereas the E_a for a-nSi oxidation remains relatively low, suggesting a different pathway.

a-nSi has shown a different oxidation behavior from c-nSi particles according to the DTG results, with low activation energy throughout the oxidation process. To probe the underlying mechanism for this behavior, DRIFTS coupled with *in situ* heating was used to monitor the oxidation of nSi particles. nSi particles were heated in synthetic air (21% O_2; 79% N_2) at $10\,°C/$min from room temperature to $\sim 550\,°C$ and DRIFTS spectra were collected during heating. In this temperature range, a-nSi has completed more than 90% of the oxidation, whereas c-nSi has only reached $\sim 20\%$ of complete oxidation according to TGA results.

Figure 5(a) shows the DRIFTS spectrum of a-nSi at room temperature. Three major regions including Si-O-Si stretching mode ($1062\,cm^{-1}$), Si-H$_x$($x = 1, 2, 3$) stretching mode (Si-$H \sim 2084\,cm^{-1}$, Si-$H_2 \sim 2010\,cm^{-1}$, Si-$H_3 \sim 2144\,cm^{-1}$), and SiO-H stretching mode ($3638\,cm^{-1}$) can be observed. These peaks indicate the presence of surface oxides, hydrides, and silanol groups on the a-nSi surface [39]. Furthermore, the zoomed-in IR spectra of the Si-H$_x$ stretching region [Fig. 5(b)] indicate that the hydride species on the a-nSi surface consist of predominantly higher hydrides, whereas the c-nSi surface contains mainly monohydride. The evolution of surface species during oxidation will be monitored to investigate the reactions involved in the low temperature oxidation of a-nSi particles.

The evolution of DRIFTS spectra of the Si-H stretching region with temperature is shown in Fig. 6(a). The peak around 2084–2144 cm^{-1} is evidence of the presence of Si-H$_x$($x = 1, 2, 3$) species on the surface of a-nSi particles. As temperature increases, this peak gradually shifts upward to 2195 cm^{-1}, and subsequently to 2250 cm^{-1}. The peaks at 2195 and 2250 cm^{-1} represent O_2Si-H_2 and O_3Si-H species, respectively [39]. The blueshift of the Si-H band is caused by electron withdrawing effect of the oxygen atom attached to the silicon atom of the Si-H bond [40]. This result indicates
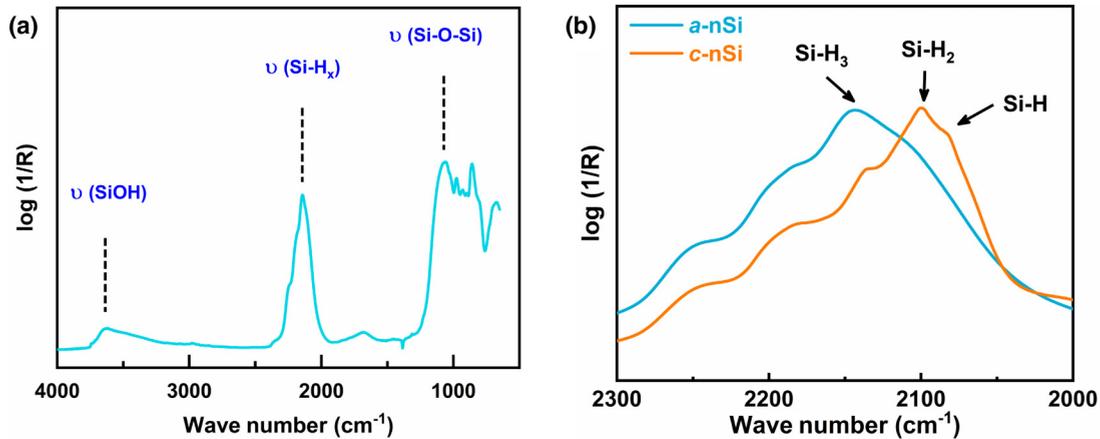
FIG. 5. (a) DRIFTS spectrum of *a*-nSi collected at room temperature. (b) Comparison of Si-H$_x$ stretching region for *a*-nSi and *c*-nSi.

that the oxidation proceeds via a backbond oxidation pathway where oxygen is inserted between adjacent Si-Si bonds instead of surface Si-H bonds [41]. From a thermodynamic perspective, the bond energy of Si-Si bond is lower than that of the Si-H bond, so it is also energetically favorable to break the Si-Si bond [42].

The temperature dependence of peak areas is plotted in Fig. 6(b). O$_2$Si-H$_2$ and O$_3$Si-H peaks start to emerge at slightly below 100 °C, similar to the oxidation onset temperature of *a*-nSi particles in TGA, indicating that the backbond pathway is responsible for the initial stage of the *a*-nSi oxidation. *c*-nSi shows an onset of ∼200 °C for O$_2$Si-H$_2$ and O$_3$Si-H peaks (see Fig. S3 of the Supplemental Material [28]), which is also consistent with TGA results. As temperature increases, surface hydrides gradually convert to O$_2$Si-H$_2$ and O$_3$Si-H. At above 320 °C, hydrogen is gradually lost due to desorption [10] and there is no sign of Si-H species above 500 °C.

The DRIFTS spectra of the Si-OH region are illustrated in Fig. 7(a), with the temperature dependence of the peak position and peak area shown in Fig. 7(b). There are two types of peaks in the spectra: a broad peak at lower wave number (3630–3690 cm^{-1}) and a sharp peak at higher wave number

(∼3735 cm^{-1}). The peak at lower frequency corresponds to associated Si-OH groups and the broadening is due to hydrogen bonding effects [39]. The peak at higher frequency represents isolated Si-OH species [43]. The results suggest that Si-OH groups start to form at below 100 °C, around the same temperature as oxygenated hydrides form. The associated Si-OH peak continues to increase until ∼340 °C, but the rate slightly decreases after 250 °C. These two temperatures also correspond to the onset temperature for the decrease of O$_3$Si-H and O$_2$Si-H$_2$, respectively. These coincident behaviors suggest that the formation of Si-OH during oxidation is related to oxygenated hydrides. Previous isotope labeling experiments have also suggested that the formation of silanol groups during the oxidation of porous silicon is a result of reaction between Si-O and Si-H bonds, instead of reaction between silicon and water [39]. At above 340 °C, the majority of the associated Si-OH groups are converted to isolated Si-OH, and the peak area starts to decrease, indicating loss of silanol groups.

The DRIFTS spectra suggest that a native oxide of *a*-nSi particles coexists with Si-H$_x$, O$_x$Si-H$_y$, and Si-OH groups. The Si-O-Si stretching mode shifted to 1078 from 1062 cm^{-1} after complete oxidation (see Fig. S4 of the Supplemental
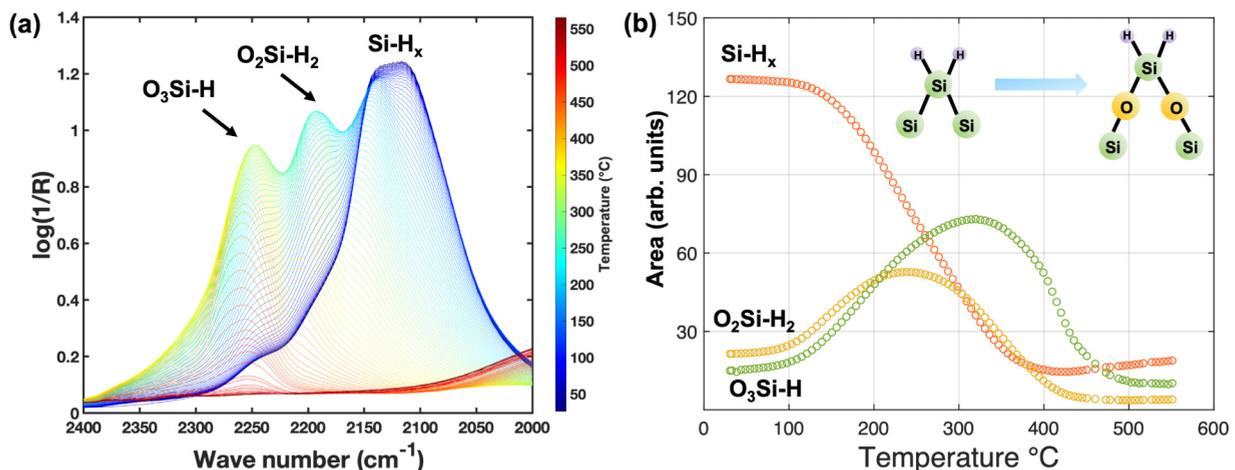
FIG. 6. (a) Evolution of Si-H$_x$ region and (b) change in peak areas of Si-H$_x$, O$_2$Si-H$_2$, and O$_3$Si-H$_3$ with temperature during oxidation of *a*-nSi. The inset illustrates the backbond oxidation mechanism.
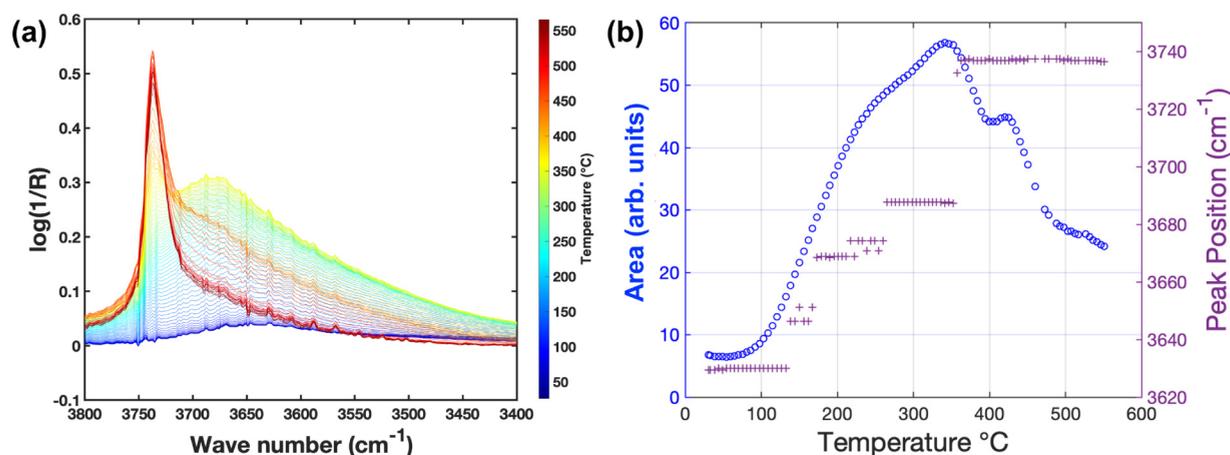
FIG. 7. (a) Evolution of Si-OH region during oxidation. (b) The change in peak position and peak area of Si-OH with temperature.

Material [28]) due to transition from substoichiometric silicon oxide to SiO_2 [44]. The shoulder peak of the room temperature spectrum between 1000 and $1050\,cm^{-1}$ also indicates the presence of substoichiometric oxide of silicon, which was confirmed by previous study using XPS and EELS [45]. However, after complete oxidation, the peaks of H-containing groups in IR spectra become minimal (as shown in Figs. 6 and 7), and the Si-O-Si stretching mode corresponding to SiO_2 is the only prominent peak left, indicating that most hydrides and silanol groups have been removed and stoichiometric oxide is formed.

The above results provided more insights on the different oxidation behaviors of *a*-nSi and *c*-nSi that was indicated by the DTG patterns. Due to the presence of abundant surface silicon hydrides, the oxidation of *a*-nSi particles proceeds primarily via backbond oxidation of silicon hydrides, along with the formation of Si-OH. This leads to a particle surface with O_3Si-H and Si-OH species, and their presence could lead to formation of suboxides and prevent the growth of a dense SiO_2 layer at low temperature. As a result, oxygen can diffuse through low energy barrier pathway to react with bulk silicon as indicated by the low temperature oxidation of *a*-nSi. The O_3Si-H and Si-OH species are further converted to silicon oxide at elevated temperature to complete oxidation. Due to lack of higher hydrides on the surface, *c*-nSi particles do not show the same low temperature oxidation behavior. The activation energy for *c*-nSi oxidation is much higher and only ~20% of oxidation occurs below 600 °C, while *a*-nSi particles complete 90% of oxidation in the same temperature range. Instead, oxidation of *c*-nSi particles undergoes a diffusion-controlled process at high temperature because of the formation of a critical oxide layer.

IV. CONCLUSIONS

The oxidation kinetics of nSi particles prepared by nonthermal plasma were studied by thermogravimetric analysis. The samples were measured at various heating rates in dry air. Results indicate that the oxidation of *a*-nSi particles undergoes a low temperature pathway and has a much lower activation energy compared to their crystalline counterparts. By applying nonisothermal kinetic analysis methods, the activation energy for oxidation onset of *a*-nSi and *c*-nSi particles was estimated by the Kissinger method to be 98 and 182 kJ/mol, respectively. The FWO method yields similar values and a critical thickness of 0.7–0.8 nm for the surface oxidation regime. *In situ* heating DRIFTS study shows that backbond oxidation of higher hydrides is responsible for the initial oxidation of *a*-nSi and the low activation energy. It appears that *a*-nSi particles do not form a dense oxide layer after surface oxidation, and therefore is able to complete oxidation at relatively low temperature compared with *c*-nSi particles. The results could be helpful for manipulating oxide growth of amorphous silicon in the thin film regime.

[1] F. Priolo, T. Gregorkiewicz, M. Galli, and T. F. Krauss, Silicon nanostructures for photonics and photovoltaics, Nat. Nanotechnol. **9**, 19 (2014).

[2] B. F. P. McVey and R. D. Tilley, Solution synthesis, optical properties, and bioimaging applications of silicon nanocrystals, Acc. Chem. Res. **47**, 3045 (2014).

[3] W. An, B. Gao, S. Mei, B. Xiang, J. Fu, L. Wang, Q. Zhang, P. K. Chu, and K. Huo, Scalable synthesis of ant-nest-like bulk porous silicon for high-performance lithium-ion battery anodes, Nat. Commun. **10**, 1447 (2019).

[4] C. H. Yang, R. C. C. Leon, J. C. C. Hwang, A. Saraiva, T. Tanttu, W. Huang, J. Camirand Lemyre, K. W. Chan, K. Y. Tan, F. E. Hudson *et al.*, Operation of a silicon quantum processor unit cell above one kelvin, Nature (London) **580**, 350 (2020).

[5] P. Ghildiyal, X. Ke, P. Biswas, G. Nava, J. Schwan, F. Xu, D. J. Kline, H. Wang, L. Mangolini, and M. R. Zachariah,

Silicon nanoparticles for the reactivity and energetic density enhancement of energetic-biocidal mesoparticle composites, ACS Appl. Mater. Interfaces **13**, 458 (2021).

[6] F. Xu, P. Biswas, G. Nava, J. Schwan, D. J. Kline, M. C. Rehwoldt, L. Mangolini, and M. R. Zachariah, Tuning the reactivity and energy release rate of I2O5 based ternary thermite systems, Combust. Flame **228**, 210 (2021).

[7] J. Schwan, B. Wagner, M. Kim, and L. Mangolini, Controlled growth of silicon particles via plasma pulsing and their application as battery material, J. Phys. Appl. Phys. **55**, 094002 (2021).

[8] P. Photopoulos, A. G. Nassiopoulou, D. N. Kouvatsos, and A. Travlos, Photoluminescence from nanocrystalline silicon in Si/SiO$_2$ superlattices, Appl. Phys. Lett. **76**, 3588 (2000).

[9] M. Ieong, B. Doris, J. Kedzierski, K. Rim, and M. Yang, Silicon device scaling to the sub-10-Nm regime, Science **306**, 2057 (2004).

[10] F. Xu, G. Nava, P. Biswas, I. Dulalia, H. Wang, Z. Alibay, M. Gale, D. J. Kline, B. Wagner, L. Mangolini *et al.*, Energetic characteristics of hydrogenated amorphous silicon nanoparticles, Chem. Eng. J. **430**, 133140 (2022).

[11] B. P. Falcão, J. P. Leitão, M. R. Soares, L. Ricardo, H. Águas, R. Martins, and R. N. Pereira, Oxidation and Strain in Free-Standing Silicon Nanocrystals, Phys. Rev. Appl. **11**, 024054 (2019).

[12] H. I. Liu, D. K. Biegelsen, F. A. Ponce, N. M. Johnson, and R. F. W. Pease, Self-limiting oxidation for fabricating sub-5 Nm silicon nanowires, Appl. Phys. Lett. **64**, 1383 (1994).

[13] R. Okada and S. Iijima, Oxidation property of silicon small particles, Appl. Phys. Lett. **58**, 1662 (1991).

[14] S. R. Kelemen, Y. Goldstein, and B. Abeles, Oxidation studies of hydrogenated amorphous silicon, Surf. Sci. **116**, 488 (1982).

[15] Z. H. Lu, E. Sacher, and A. Yelon, Kinetics of the room-temperature air oxidation of hydrogenated amorphous silicon and crystalline silicon, Philos. Mag. B **58**, 385 (1988).

[16] B. Drevillon and F. Vaillant, Oxidation of plasma-deposited hydrogenated amorphous silicon, Thin Solid Films **124**, 217 (1985).

[17] M. Y. Bashouti, K. Sardashti, J. Ristein, and S. H. Christiansen, Early stages of oxide growth in H-Terminated silicon nanowires: determination of kinetic behavior and activation energy, Phys. Chem. Chem. Phys. **14**, 11877 (2012).

[18] X. Zhang, Y. Duan, X. Dai, T. Li, Y. Xia, P. Zheng, H. Li, and Y. Jiang, Atomistic origin of amorphous-structure-promoted oxidation of silicon, Appl. Surf. Sci. **504**, 144437 (2020).

[19] J. Holm and J. T. Roberts, Thermal oxidation of 6 Nm aerosolized silicon nanoparticles: Size and surface chemistry changes, Langmuir **23**, 11217 (2007).

[20] J. Salonen, V.-P. Lehto, and E. Laine, Thermal oxidation of free-standing porous silicon films, Appl. Phys. Lett. **70**, 637 (1997).

[21] B. E. Deal and A. S. Grove, General relationship for the thermal oxidation of silicon, J. Appl. Phys. **36**, 3770 (1965).

[22] Y. Enta, B. S. Mun, M. Rossi, P. N. Ross, Z. Hussain, C. S. Fadley, K.-S. Lee, and S.-K. Kim, Real-time observation of the dry oxidation of the Si(100) surface with ambient pressure x-ray photoelectron spectroscopy, Appl. Phys. Lett. **92**, 012110 (2008).

[23] Y.-C. Liao, A. M. Nienow, and J. T. Roberts, Surface chemistry of aerosolized nanoparticles:thermal oxidation of silicon, J. Phys. Chem. B **110**, 6190 (2006).

[24] N. Gayathri and S. Banerjee, Layering of ultrathin SiO$_2$ film and study of its growth kinetics, Appl. Phys. Lett. **84**, 5192 (2004).

[25] H. E. Kissinger, Reaction kinetics in differential thermal analysis, Anal. Chem. **29**, 1702 (1957).

[26] J. H. Flynn and L. A. Wall, General treatment of the thermogravimetry of polymers, J. Res. Natl. Bur. Stand. Sect. Phys. Chem. **70A**, 487 (1966).

[27] T. Ozawa, A new method of analyzing thermogravimetric data, Bull. Chem. Soc. Jpn. **38**, 1881 (1965).

[28] See Supplemental Material at http://link.aps.org/supplemental/10.1103/PhysRevMaterials.7.045403 for illustration of experimental setup for the nonthermal plasma synthesis of nSi particles, TEM analysis of crystalline nSi particles, DRIFTS result of change in peak areas of Si-H$_x$, O$_2$Si-H$_2$, and O$_3$Si-H with temperature during oxidation of *c*-nSi, and Si-O-Si stretching region of DRIFTS spectra of *a*-nSi at room temperature and 500 °C.

[29] L. Mangolini, E. Thimsen, and U. Kortshagen, High-yield plasma synthesis of luminescent silicon nanocrystals, Nano Lett. **5**, 655 (2005).

[30] U. R. Kortshagen, R. M. Sankaran, R. N. Pereira, S. L. Girshick, J. J. Wu, and E. S. Aydil, Nonthermal plasma synthesis of nanocrystals: Fundamental principles, materials, and applications, Chem. Rev. **116**, 11061 (2016).

[31] P. Agarwal and S. L. Girshick, Numerical modeling of an RF argon–silane plasma with dust particle nucleation and growth, plasma chem, Plasma Process. **34**, 489 (2014).

[32] L. Mangolini and U. Kortshagen, Selective nanoparticle heating: Another form of nonequilibrium in dusty plasmas, Phys. Rev. E **79**, 026405 (2009).

[33] T. Lopez and L. Mangolini, Low activation energy for the crystallization of amorphous silicon nanoparticles, Nanoscale **6**, 1286 (2014).

[34] S. Ye, K. Yamabe, and T. Endoh, Oxidation of silicon nanopillars, J. Phys. Chem. C **125**, 8853 (2021).

[35] S. Vyazovkin, A. K. Burnham, J. M. Criado, L. A. Pérez-Maqueda, C. Popescu, and N. Sbirrazzuoli, ICTAC kinetics committee recommendations for performing kinetic computations on thermal analysis data, Thermochim. Acta **520**, 1 (2011).

[36] S. Vyazovkin, Kissinger method in kinetics of materials: Things to beware and be aware of, Molecules **25**, 12 (2020).

[37] C. D. Doyle, Estimating isothermal life from thermogravimetric data, J. Appl. Polym. Sci. **6**, 639 (1962).

[38] M. Morita, T. Ohmi, E. Hasegawa, M. Kawakami, and M. Ohwada, Growth of native oxide on a silicon surface, J. Appl. Phys. **68**, 1272 (1990).

[39] D. B. Mawhinney, J. A. Glass, and J. T. Yates, FTIR study of the oxidation of porous silicon, J. Phys. Chem. B **101**, 1202 (1997).

[40] A. Borghesi, G. Guizzetti, A. Sassella, O. Bisi, and L. Pavesi, Induction-model analysis of SiH Stretching Mode In Porous Silicon, Solid State Commun. **89**, 615 (1994).

[41] B. N. Jariwala, N. J. Kramer, M. C. Petcu, D. C. Bobela, M. C. M. van de Sanden, P. Stradins, C. V. Ciobanu, and S. Agarwal, Surface hydride composition of plasma-synthesized Si nanoparticles, J. Phys. Chem. C **115**, 20375 (2011).

[42] R. Walsh, Bond dissociation energy values in silicon-containing compounds and some of their implications, Acc. Chem. Res. **14**, 246 (1981).

[43] B. A. Morrow and I. A. Cody, Infrared spectra of the isolated hydroxyl groups on silica, J. Phys. Chem. **77**, 1465 (1973).

[44] J. Lambers and P. Hess, Infrared spectra of photochemically grown suboxides at the Si/SiO_2 interface, J. Appl. Phys. **94**, 2937 (2003).

[45] B. J. Winters, J. Holm, and J. T. Roberts, Thermal processing and native oxidation of silicon nanoparticles, J. Nanoparticle Res. **13**, 5473 (2011).